INSTITUTE OF PHYSICS PUBLISHING JOURNAL OF MICROMECHANICS AND MICROENGINEERING

J. Micromech. Microeng. **15** (2005) 812–821 doi:10.1088/0960-1317/15/4/020

A lobster-sniffing-inspired method for micro-objects manipulation using electrostatic micro-actuators

Chieh Chang[1], Chia-Fang Chiang[1], Cheng-Hsiang Liu[1] and Cheng-Hsien Liu[1,2]

[1] Department of Power Mechanical Engineering, National Tsing-Hua University, Hsinchu, Taiwan 30043, Republic of China
[2] Institute of Microelectromechanical Systems, National Tsing-Hua University, Hsinchu, Taiwan 30043, Republic of China

E-mail: liuch@pme.nthu.edu.tw

Received 15 November 2004, in final form 19 January 2005
Published 25 February 2005
Online at stacks.iop.org/JMM/15/812

Abstract
We learn from nature to mimic, from the viewpoint of controlling Reynolds number variations, the odor-molecule capturing function of lobsters' tiny hairs on their antennules for finding food, a suitable mate or to avoid predators to capture molecules from the surrounding fluid. The engineering implementation of this lobster-hair-like capturing device, which is actuated by the electrostatic force, is reported in this paper. The device actuates and drives the biological objects via disturbing the fluid field and manipulating the Reynolds number of the surrounding fluid to achieve the function of micro-object manipulation. The operation principle of this micro-object manipulation is very different from those of other researchers' early work such as MEMS ciliary actuators. In this paper, both theoretical analyses and simplified numerical simulations are presented to obtain the design criteria as well as the microfabrication processes. Preliminary experimental results are also shown to demonstrate the feasibility and functionality via the micro-object manipulation in liquid environment. These biomimetic electrostatic bimorph actuators could avoid some of the drawbacks of conventional tools and are potential tools for the non-contact and non-invasive manipulation of micro/nano bio-objects.

(Some figures in this article are in colour only in the electronic version)

1. Introduction

Manipulation of bio-objects is an important subject for bio-medical research [1]. There are many efforts dedicated to the development of tools for the manipulation of bio-objects. Conventional approaches employ pipettes to manipulate bio-objects. This method requires precise control and positioning of the pipette to manipulate a single cell, which is a highly specialized, labor-intensive task. Optical tweezers [2] have the advantage of easy manipulation and are widely used. However, the equipment is expensive compared to other techniques. Meanwhile, with the development of micromachining technology, numerous micro-manipulation tools have been proposed based on different transducers such as electromagnetic actuators [3], electrostatic actuators [4] and thermal-bimorph actuators [5–8]. Among these researches, most actuators serve as micro-conveyors based on ciliary motion for small-object manipulation. When it comes to bio-object manipulation, the microgripper [9, 10], the microcage [11] and the conjugated polymer actuator [12] are based on clamping mechanisms to grab bio-objects. A popular way of trapping cells using dielectrophoresis (DEP) is growing fast and their capabilities for the manipulation of micro-beads have been proved [13]. The extension for the manipulation of different live cells by using DEP is still a challenge in this research field.

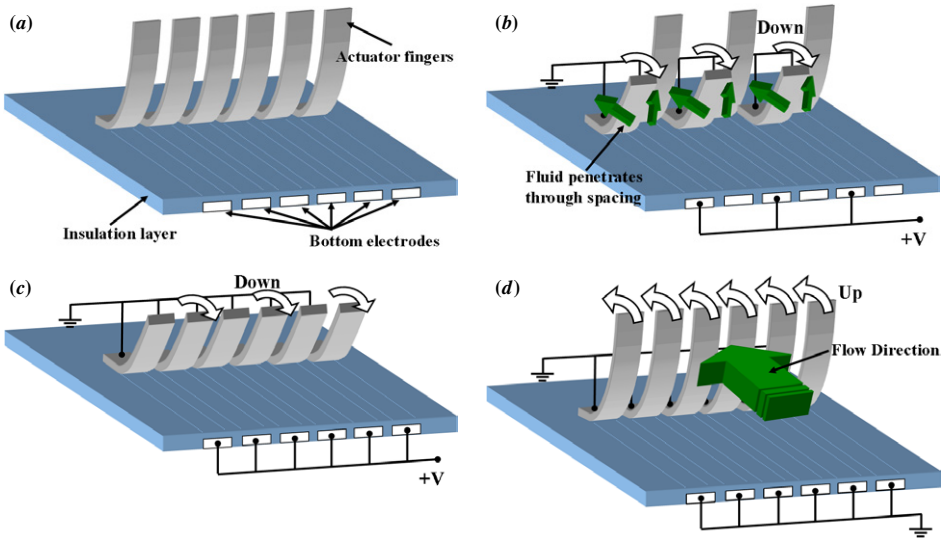

Figure 1. Schematic illustration of the electrostatic micro-actuators: (*a*) overview of the actuator; (*b*) voltage is applied to move down half of the fingers first; (*c*) the rest of the fingers are moved down; (*d*) the voltage is removed and the fingers return to their original position.

In this paper, an innovative idea is proposed, which mimics the capturing function of lobsters' tiny hairs on their antennules (i.e. the second pair of antennae on the head of a crustacean) to control the fluid surrounding the targeted objects in order to catch them. The technique development on MEMS bimorph cantilevers and electrostatic cantilever actuators is exploited to develop the curved-finger actuator, a lobster-hair-like capturing actuator. The moving mechanism might look like the early ciliary motion research [3–8]. However, the operation principle of our micro-object manipulation is very different from those of early ciliary motion research. Our device actuates and drives the micro-objects via disturbing the fluid field and manipulating the Reynolds number of the surrounding fluid to achieve the function of micro-object manipulation. These biomimetic electrostatic micro-actuators could avoid some of the drawbacks of conventional tools and target to be suitable for some bio-medical applications, such as parallel cell-patterning for liver tissue engineering, in the future.

2. The lobster-sniffing-inspired method

2.1. Learn from nature

For centuries, engineers have looked at nature for inspiration. The original idea of this research should thank Kohl *et al* who have done excellent work on the research of how lobsters sniff [14]. Their extensive work has indicated that capturing odor molecules from the surrounding fluid allows lobsters to employ their sense of smell for biologically critical activities such as finding food, mates or habitats. The function of a lobster's antennules system can be classified into two stages: bring the targeted particles near their tiny hairs by controlling the Reynolds number of the surrounding fluid, which is a kind of non-contact manipulation, and then get in touch with the particle to smell. From the experiments of Kohl and co-workers, it was found that lobsters can transfer chemosensory hairs, on the end of their antennules, from a leaky filter mode to a non-leaky paddle mode via the antennules' stroke velocity (i.e. the relative velocity of swung antennules and liquid). This could be explained using the concept of Reynolds number ($Re = ul/\nu$, where u is the velocity, l is the characteristic length and ν is the kinematic viscosity), which represents the relative importance of inertial to viscous force in a moving fluid flow. Because the fluid in contact with the surface of a moving body does not slip relative to the body, a velocity gradient, or say boundary layer, would develop around the body. The lower the Re (i.e. the smaller the body or slower the velocity), the thicker this boundary layer is relative to the body. If the boundary layer is thicker than the spacing between the two bodies, the spacing will be clogged. This case is a paddle mode. In contrast, the higher the Re (i.e. the bigger the body or faster the velocity), the thinner this boundary layer is relative to the body. When the boundary layer is thinner than the spacing between the two bodies, the fluid will flow smoothly through the spacing. This case is a filter mode. This effect is harnessed to design our electrostatic micro-actuators.

2.2. Structure design

Figure 1(*a*) shows the schematic illustration of our electrostatic micro-actuators design. The manipulation principle of micro-objects for our micro-actuators mimics the capturing function of lobsters' tiny hairs on its antennules from the viewpoint of controlling Reynolds number variations. These micromachined micro-actuator fingers have similar dimensions to those of the lobster's tiny hairs but with some dimension modification based on numerical simulation results to meet real operation conditions or limitations from the viewpoint of engineering approach. The whole device consists of bottom electrodes and a row of curled actuator fingers. The curled fingers are connected to the ground electrode. All the bottom electrodes are buried under an insulation layer to isolate them from the liquid environment and to prevent electrical short contact with the actuator fingers. The bimetal actuator fingers curl up due to the bimorph effect after the release process. When the voltage is applied to the bottom electrodes, the corresponding actuator fingers would be pulled

down by electrostatic force and then zip along the bottom electrodes as the voltage increases, until the actuator fingers are pulled to be flat. In contrast, when the voltage is removed, the corresponding actuator fingers would curl up back to their original shape. The actuator fingers are in an array to serve as the structures to control the fluid field. During operation, the voltage is first applied on the odd bottom electrodes and the corresponding actuator fingers are pulled down fast, as illustrated in figure 1(*b*). For this case, fluid can penetrate through the larger spacing between the actuator fingers. The voltage is then applied on the even bottom electrodes to pull down the rest of the actuator fingers, as illustrated in figure 1(*c*). Finally, as illustrated in figure 1(*d*), the voltage is gradually removed and all the actuator fingers return to their original positions simultaneously. In this case, the actuator fingers have lower velocity and smaller spacing in-between to result in fluid motion and consequently draw the targeted object near. Based on the demand, a row of actuator fingers could be transferred from a paddle mode to a filter mode via fine tuning and control of actuator finger width, spacing and velocity, and vice versa.

3. Theoretical analysis and simulation

The following section will discuss the relevant theory involved in analyzing these actuators and the fluid field around them.

3.1. Curled fingers

The actuator fingers are curled up after the release process via the residual stress mismatch of the bimetallic layers. Residual stress is a fundamental problem associated with the deposition of thin film. For proper exploitation, this inherent nature of bimetal thin film is utilized to curl up the actuator fingers spontaneously after release.

The relationship between the radius of curvature, ρ, and the residual stress, σ, can be expressed as (1) [15, 16]

$$\rho = \frac{E_2 h(3m + k/n(1+n)^2)}{6(m\sigma_2 - \sigma_1)} \tag{1}$$

and

$$k = 1 + 4mn + 6mn^2 + 4mn^3 + m^2n^4 \tag{2}$$

where E_1 and E_2 are Young's moduli of the first and second thin-film layers, respectively, $h = h_1 + h_2$ is the total thickness of the bimetallic layers with the first layer thickness of h_1 and the second layer thickness of h_2, $m = E_1/E_2$ and $n = h_1/h_2$. For our design, the bottom layer is set to be aluminum and the upper layer is set to be chromium. The values of E_1 (Al) and E_2 (Cr) are 70.3 GPa and 140 GPa, respectively[3]. The value of $m\sigma_2 - \sigma_1$, substantially depending on the fabrication process, is measured to be 1.0 GPa for our device. Figure 2 shows the calculation results of the curvature radius, ρ, as a function of the thickness ratio of chromium to aluminum, h_2/h_1, with different aluminum thicknesses, h_1.

The radius of curvature decreases with the film thickness ratio. When the film thickness ratio h_2/h_1 is larger than some value, say 0.1, for the case of Al = 0.8 μm, the changing rate

[3] Young's moduli values of aluminum and chromium are used from the database of MEMCAD, design tools from Conventor, Inc.

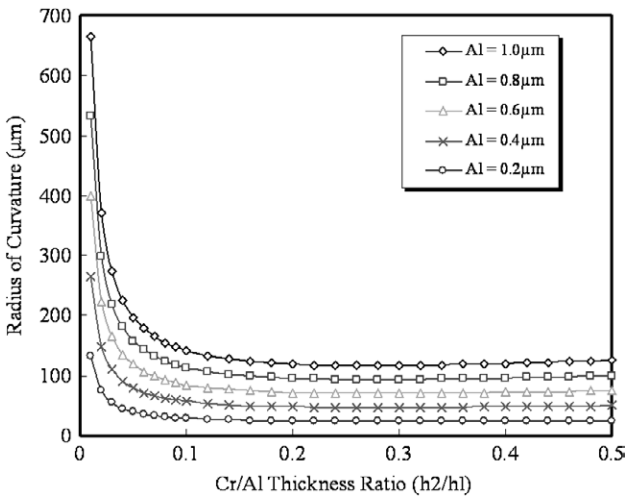

Figure 2. Plot of the calculated radius of curvature versus the thickness ratio for different aluminum thickness.

is very slow. The above observation only holds for the range of film thickness ratio h_2/h_1 presented in figure 2. When the film thickness ratio h_2/h_1 gets much higher beyond our focus region, which is not shown in figure 2, the curve will rise with a sharp slope. The minimum value of the curvature radius versus the Cr/Al thickness ratio variation could be obtained. Note that the slope for the decrease rate is steep when the thickness ratio is below 0.1 for the case of Al = 0.8 μm. The curvature is difficult to control in this region by the thickness ratio due to fabrication variation error and non-uniformity deposition.

Furthermore, the radius of curvature decreases as the aluminum thickness, h_1, decreases. To achieve a smaller radius of curvature to curl up actuator fingers, thinner aluminum layer is required. However, thinner thickness also means lower stiffness. It should be pointed out that the analytical solution, equation (1), will fail when the radius of curvature, ρ, gets very small. This results in some errors for the curvature radius design of our curled finger actuator. In the next section, the stiffness of the fingers regarding different finger dimensions via modal analysis will be analyzed to obtain the optimal design of finger thickness.

3.2. Vibration modes

The individual thickness and ratio of bimetal layers dominate the curling shape of our micro-actuator fingers. Structure dimensions of bimetal layers affect the stiffness of the fingers as well as the vibration mode. The curling shape and structure dynamics couple in our micro-actuators to complicate our design. The MEMS software package, CoventorWare, is used to perform modal analysis and to give us more insight about the dimension effect. From modal analysis, the resonant frequencies as well as the stiffness of the actuator fingers could be obtained.

Because the chromium layer is so thin compared with the aluminum layer, the stiffness effect of the chromium layer could be ignored. The dimensions of aluminum structure in our simulation model are 200 μm in radius of curvature, 5 μm in width and 0.8 μm in thickness. Young's modulus, Poisson's ratio and density of aluminum are set to be

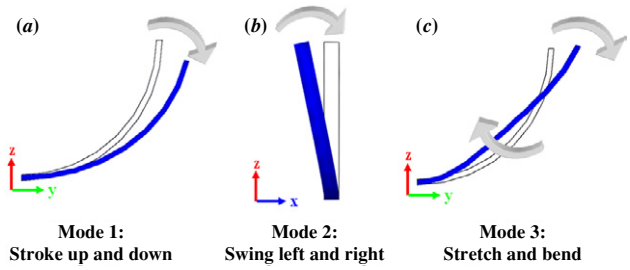

Figure 3. Schematic illustration of the vibration modes.

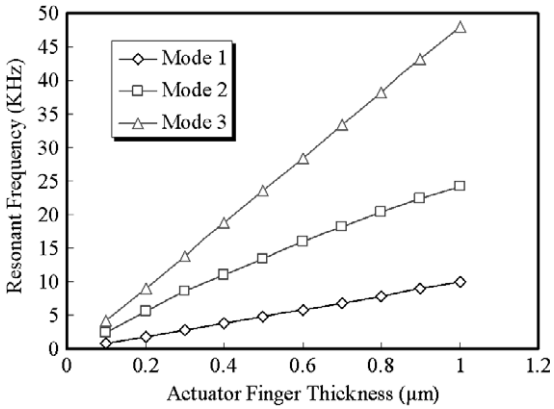

Figure 4. Plot of the simulation results of vibration resonance versus actuator finger thickness.

7.0×10^4 (MPa), 0.3 and 2.3×10^{-15} (kg μm^{-3}), respectively. Our curl-shape actuator fingers will be tested and operated in a liquid environment eventually. Here, to simplify the complication, the liquid effects are not considered in the computer-aided simulation for all modal analyses. The practical liquid operation environment would increase the damping effect and might push the resonant dynamics to a higher resonant frequency. Figure 3 shows the simulation result of the first three vibration modes. The first vibration mode is stroking up and down mode, the second mode is swinging left and right mode and the third mode is stretching and bending mode. The first vibration mode is the mode which the actuator fingers are targeted to be operated under. Thus, in our design, higher vibration modes far away from the first vibration mode are required to prevent the undesired coupling effect from higher vibration modes. Figure 4 shows that the slope of the first vibration resonant frequency versus actuator finger thickness is smaller than those of higher order vibration resonant frequencies. Here, the parameters in the simulation remain the same except the thickness. This result indicates that an increase of the actuator finger thickness in our design could minimize the dynamic coupling effect of higher vibration modes while the actuator fingers operate under the first vibration resonance. Besides, as the actuator finger thickness increases, the finger stiffness also increases. Figure 5 shows that the actuator finger width has little effect on the resonant frequencies of modes 1 and 3 as well as actuator finger stiffness. The resonant frequency of mode 2 is proportional to the actuator finger width. This result implies that the actuator finger width is a less independent and least constrained design parameter for the dynamics of the actuator

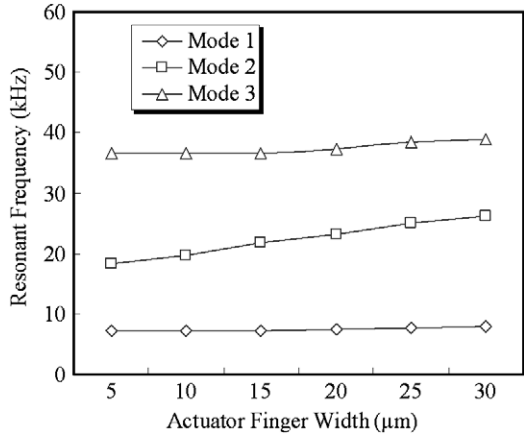

Figure 5. Plot of the simulation results of vibration resonance versus actuator finger width.

fingers. However, the actuator finger width is an important parameter for mimicking lobster's tiny-hairs function in fluid field analysis which will be described later.

Figure 4 shows the simulation results for resonant frequencies versus the actuator finger thickness of 0.1–1 μm. The resonant frequency of the first vibration mode is 834 Hz for the actuator fingers of 0.1 μm thickness. It is little bit low and soft because the actuator fingers are targeted to operate in a liquid environment at frequencies higher than 1 kHz to obtain the high actuator finger velocity relative to the fluid. Therefore, a finger thickness larger than 0.1 μm is required in our design. In any case, the payoff for the thick actuator finger is a large actuating voltage. This issue will be addressed in the later section. The fluid damper in our simulation is neglected since it is difficult to estimate especially in the micro-scale. The main approach is to design the actuator finger with a vibration frequency high enough to allow the actuator fingers to operate at high speed in the fluid environment.

3.3. Driving voltage

A two-dimensional model based on the Rayleigh–Ritz method and small deformation theory is built up for the investigation of driving voltage. When a dc voltage is applied on the bottom electrode, the total potential energy, π, can be expressed as [17]

$$\pi = U_{\mathrm{b}} + V_{\mathrm{el}} \tag{3}$$

where U_{b} and V_{el} are the bending strain energy and the electrostatic potential energy, respectively, given by [17, 18]

$$U_{\mathrm{b}} = \frac{1}{2}\int_0^L EI\left[\frac{\mathrm{d}^2\omega(x)}{\mathrm{d}x^2}\right]^2 \mathrm{d}x \tag{4}$$

and

$$V_{\mathrm{el}} = -\frac{1}{2}\int_0^L \frac{\varepsilon_0 W V^2}{(g/\varepsilon_1) + (y(x)/\varepsilon_2)}\mathrm{d}x. \tag{5}$$

The parameters above are shown in figure 6. Here EI is the bending stiffness of the finger, $\omega(x) = f(x) - y(x)$ is the static deflection, $f(x)$ is the original shape of the curled finger as a function of position x, $y(x)$ is the deflection of the curled finger as a function of position x, ε_0 is the dielectric constant of free space, ε_1 is the dielectric constant of the insulation

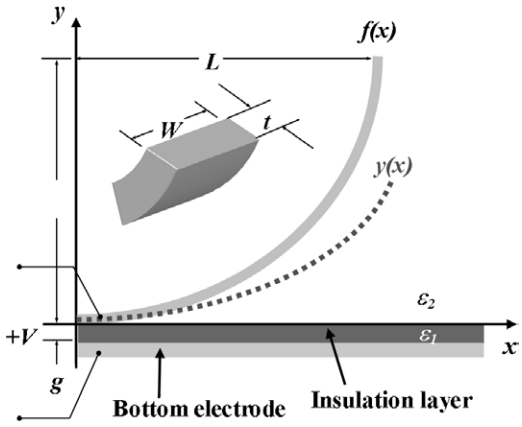

Figure 6. Two-dimensional model of curled finger for our simulation.

layer, ε_2 is the dielectric constant of the environment, W is the finger width, V is driving voltage and g is the insulation layer thickness.

The potential energy π can be obtained as

$$\pi = 72EIa^2\int_0^L (x-L)^4 \mathrm{d}x - \frac{\varepsilon_0\varepsilon_1\varepsilon_2 W V^2}{2}\int_0^L \frac{\mathrm{d}x}{\varepsilon_2 g + \varepsilon_1 y(x)}, \tag{6}$$

where a is a constant to be determined. The pull-in voltage of the finger, V_{PI}, can thus be acquired and the constant a_{PI} at pull-in is

$$V_{\mathrm{PI}}^2 = \frac{12t^3EL^5}{5\varepsilon_0\varepsilon_1^3\varepsilon_2} \times \frac{1}{\int_0^L ((x^4-4Lx^3+6L^2x^2)^2/[\varepsilon_2 g+\varepsilon_1 y(x)]^3)\mathrm{d}x} \tag{7}$$

$$a_{\mathrm{PI}} = -\frac{1}{2\varepsilon_1} \times \frac{\int_0^L ((x^4-4Lx^3+6L^2x^2)/[\varepsilon_2 g+\varepsilon_1 y(x)]^2)\mathrm{d}x}{\int_0^L ((x^4-4Lx^3+6L^2x^2)^2/[\varepsilon_2 g+\varepsilon_1 y(x)]^3)\mathrm{d}x}. \tag{8}$$

Equations (7) and (8) show the effects of different parameters. The finger width, W, would not affect the pull-in voltage. Changing the finger bending stiffness, EI, finger width, W, and thickness, t, does not contribute to the maximum displacement before pull-in.

It is hard to get the closed form solution for the equations of this system; therefore, a numerical approach is used alternatively. Figure 7 shows the calculation results for the tip displacement as a function of applied voltage for a different set of finger thicknesses. As the finger thickness increases, the pull-in voltage increases while the tip displacements just before pull-in are about the same value of 65 μm. The reason for this is that thinner finger thickness results in softer structure, i.e. lower stiffness, and lower applied voltage for the pull down of the fingers. When the applied voltage is increased, the finger is pulled down toward the position just before pull-in, which is determined by ε_1, ε_2, g, L and δ. Besides, it is also determined by the polynomial order of original shape of the curled finger [17], but it is not a controllable parameter in this study. After the critical position is passed, the bending stress

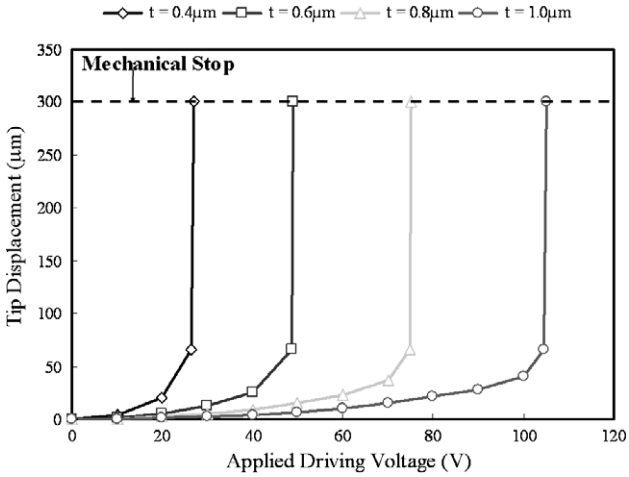

Figure 7. Plot of the calculated tip displacement versus voltage for a different set of finger thicknesses t. Parameters that have been used in our simulation are $L = 300$ μm, $\delta = 300$ μm, $E = 70.3$ GPa, $g = 0.2$ μm, $\varepsilon_0 = 8.85\times10^{-12}$, $\varepsilon_1 = 4.5$ (SiO_2), $\varepsilon_2 = 1$ (air).

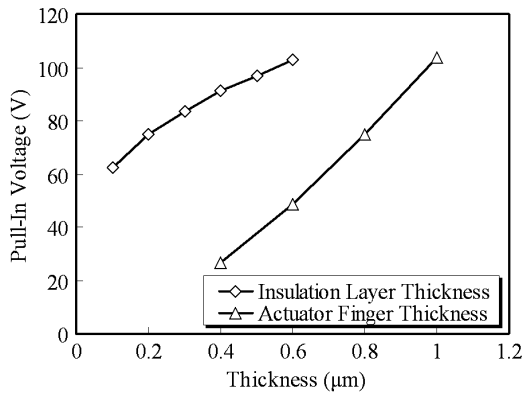

Figure 8. Plot of the calculated pull-in voltage versus the film thickness. Parameters that have been used in our simulation are t (as g varies) $= 0.8$ μm, g (as t varies) $= 0.2$ μm, $L = 300$ μm, $\delta = 300$ μm, $E = 70.3$ GPa, $g = 0.2$ μm, $\varepsilon_0 = 8.85\times10^{-12}$, $\varepsilon_1 = 4.5$ (SiO_2), $\varepsilon_2 = 1$ (air).

cannot balance the electrostatic force and the finger pulls in immediately.

The effect of the insulation layer thickness, g, and the finger thickness, t, on the pull-in voltage, V_{PI}, is also studied. Figure 8 shows the calculation results of the pull-in voltage as a function of the film thickness. Both lines are linear and have similar slope. It means that these two parameters, g and t, carry the same effect weighting on the pull-in voltage.

3.4. Fluid field

The design for our micro-actuators is critical to determine whether the fluid could penetrate through a row of actuator fingers or not. For the lobster case [20], the characteristic diameter of chemosensory hairs on its antennules is 1 μm and the ambient velocity ranges from 0.001 to 0.5 m s^{-1}. Using numerical simulation software (CFDRC^{TM}), lobsters' tiny hairs and their function are imitated to design our actuator fingers and operate them in the similar circumstance as lobsters' to get more insight into the effects of different parameters.

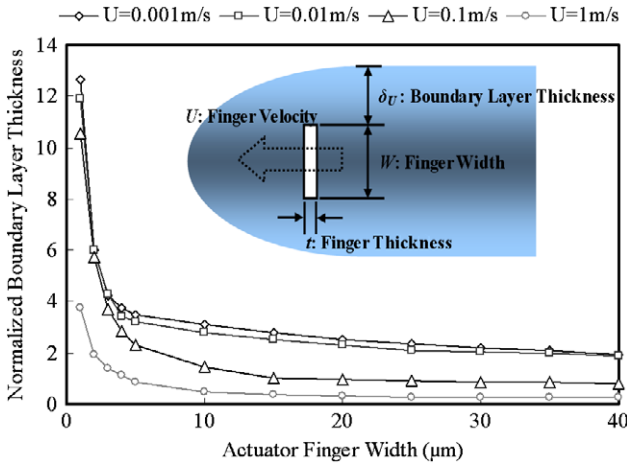

Figure 9. Plot of the simulation results of the normalized boundary layer thickness, δ_U/W, versus the actuator finger width, W, for different finger velocities, U.

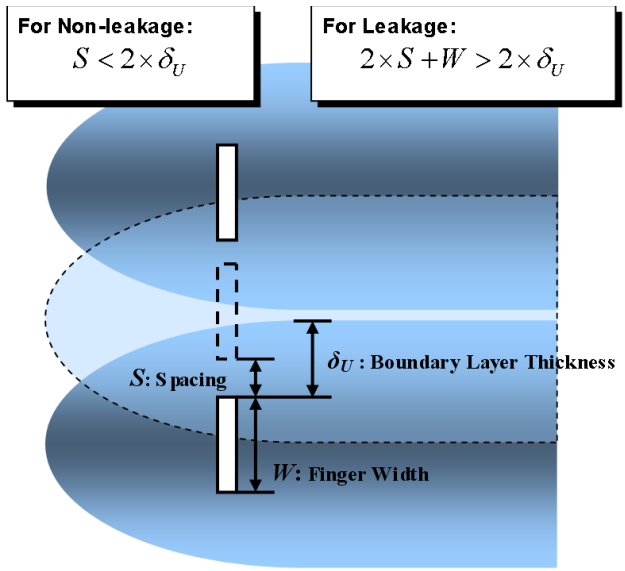

Figure 10. Schematic illustration of how to determine the spacing.

We start from studying how the boundary layer of a single actuator finger, δ_U, is affected by the actuator finger width, W, and the actuator finger velocity relative to the ambient flow, U. To mimic lobsters' tiny hairs and also achieve high mechanical stiffness for functioning in water, the actuator finger thickness, t, is modified and fixed to 0.8 μm for the current design. Figure 9 shows the simulation results for the normalized boundary layer thickness on the actuator finger, δ_U/W, as a function of the actuator finger width under different actuator finger velocities relative to ambient flow. The inset shows the cross-section of a single actuator finger passing through the fluid with velocity U. The shadow region represents the boundary layer and δ_U is the boundary layer thickness that is defined as the thickness where the velocity at the boundary layer equals the ambient velocity. The normalized boundary layer thickness decreases with the actuator finger width and velocity. This phenomenon gets more obvious and sensitive when the actuator finger width is less than 5 μm. The simulation results on the dimensional characteristics are consistent with the lobsters' natural system.

Furthermore, important information for designing the width and spacing, S, of our actuator fingers could be obtained from figure 9. As illustrated in figure 10, in the design $S < 2 \times \delta_U$, when a row of actuator fingers move simultaneously, the actuator fingers function like a paddle. In this case, the spacing between the actuator fingers is clogged. For the other case, when only either odd or even fingers move simultaneously, the row of actuator fingers behave like a filter. In that case, the fluid leaks between the actuator fingers because they satisfy the design criterion of $2 \times S + W > 2 \times \delta_U$. When the actuator finger width is well designed (by mask design) and the velocity of the actuator fingers is well controlled (by input voltage), the boundary layer thickness could be manipulated and the acceptable range of spacing design could also be acquired. For the device 5 μm in width and 5 μm in spacing, when all fingers are driven simultaneously at a velocity of 0.01 m s^{-1}, the boundary layer of each actuator finger is approximately 15 μm (see figure 9), which is thick enough to clog a 5 μm spacing. Figure 11(a) shows the computer simulation result for this case—the fluid could not penetrate through the spacing. However, when only either odd or even fingers are driven

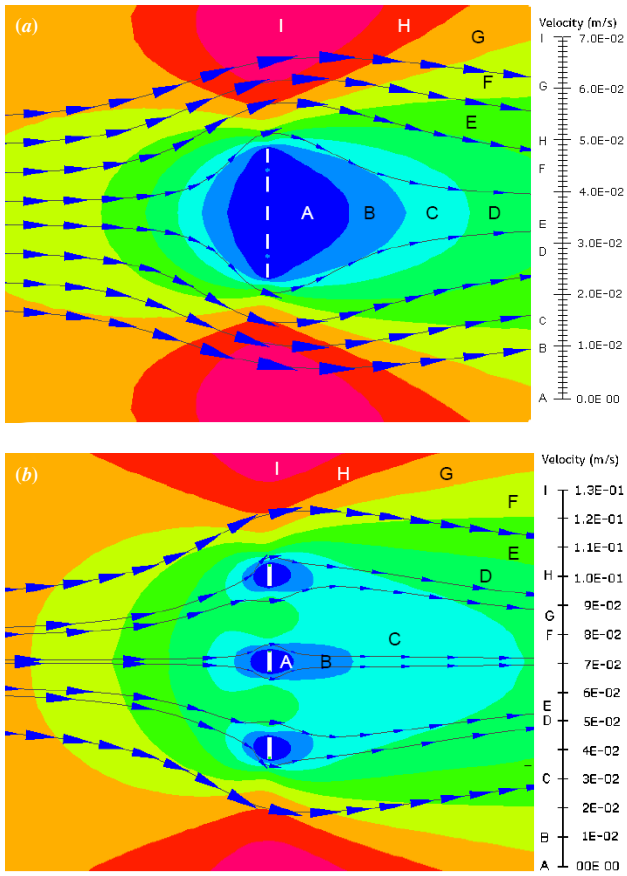

Figure 11. Numerical simulation of fluid field around a row of actuator fingers. (a) The actuator fingers are separated by 5 μm. The ambient flow velocity U is 0.01 m s^{-1}. Little fluid can penetrate through the spacing between the actuator fingers. (b) The actuator fingers are separated by 15 μm. The ambient flow velocity U is 1 m s^{-1}. Fluid would penetrate through the spacing between the actuator fingers.

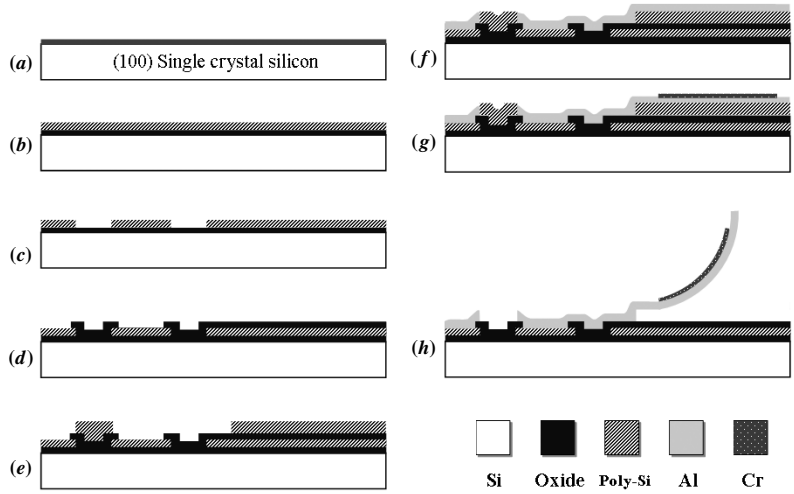

Figure 12. Process flow diagram for the electrostatic micro-actuators fabrication using five masks.

simultaneously at a velocity of 1 m s^{-1}, the boundary layer of each actuator finger is approximately 5 μm (see figure 9), which cannot clog the 15 μm spacing. Figure 11(*b*) shows the numerical simulation result for this case—the fluid can penetrate through the spacing. In figure 11, a row of actuator fingers (white strips) are 5 μm in width and 0.8 μm in thickness. The flow velocity in a different zone, $A \sim I$, is approximated and can be referred to in the legend. The lines with arrows represent the stream lines. To reduce heavy computation on simulation, the flow velocity U is assumed for the ambient fluid instead of the moving actuator fingers.

4. Fabrication

The fabrication of our micro-actuators is a five-mask process, as illustrated in figure 12. On a standard p-type ⟨1 0 0⟩ silicon wafer, 5000 Å thermal oxide is grown as the insulation layer, as shown in figure 12(*a*). This is followed by the deposition of 3000 Å LPCVD poly-silicon and phosphorus doping of poly-silicon layer to lower its resistance, as shown in figure 12(*b*). The poly-silicon layer is patterned using the RIE process to form the ground and bottom electrodes, electrical wires and electrode pads, as shown in figure 12(*c*). Here, doped poly-silicon is chosen instead of metal for the bottom drive electrode because the post-fabrication process (LPCVD) is not allowed after metal for our clean-room facility. A 2000 Å TEOS oxide layer is conformally deposited by PECVD and serves as the second insulation layer to seal the electrodes and electrical wires. The PECVD oxide layer is patterned using BOE solution to form the electrode contacts, as shown in figure 12(*d*). Then, 4000 Å LPCVD poly-silicon is deposited as the sacrificial layer. This is followed by anchor etching using the RIE process, as shown in figure 12(*e*). This step is crucial for our device. If poly-silicon cannot be removed completely, the poly-silicon residue will delaminate the fingers from anchor after the release process. If the etch time is prolonged such that the poly-silicon is completely removed, the oxide layer beneath the sacrificial layer of poly-silicon might be etched out. This would short the circuit. Besides, the non-uniformity of film deposition and RIE etching make this step more difficult.

Next, metal layers, which act as our actuator fingers, are lifted off using thick photoresist AZ9260. AZ9260 provides enough thickness (6–8 μm) and vertical shape. Both are key issues for successful lift-off. Afterwards, an 8000 Å aluminum layer is evaporated by thermal evaporation coater and is lifted off in acetone, as shown in figure 12(*f*). Similarly, a 1000 Å Cr layer, which serves as the second metal layer, is evaporated by E-Gun evaporation and is then lifted off in acetone, as shown in figure 12(*g*). The last step, as shown in figure 12(*h*), is when all exposed poly-silicon is removed via XeF_2 to release actuator fingers. XeF_2 is a gas phase etchant that etches silicon isotropically. Furthermore, XeF_2 etching would avoid stiction problems associated with wet etching and would not attack metals. The etching rate of XeF_2 mainly depends on the number of loaded samples and the size of the open etching area. The more the loaded samples have, the slower XeF_2 etches. The larger the open etching area is, the faster it etches.

5. Experimental results

5.1. Fabrication results

Figures 13(*a*) and (*b*) show two different actuator finger shapes with two different Cr/Al thickness ratios. Based on equation (1), the curvature of the fingers could be tuned by different thickness ratio of metal films. Figure 13(*a*) shows the SEM images of curled actuator fingers, which are 5 μm in width, 5 μm in spacing and 100 μm in radius of curvature. These fingers are fabricated by depositing a 0.8 μm Al film first and then a 0.1 μm Cr film. Figure 13(*b*) shows the SEM images of vertically standing actuator fingers, which are 20 μm in width, 10 μm in spacing and 300 μm in radius of curvature, with a 0.8 μm Al film and a 0.015 μm Cr film. By using FLX-2320 (KLA-Tencor, USA), the residual stress of the metal films is measured. A laser scan over the surface and determination of the reflection angle allow calculating the stress from the measured radius. With the measurements on these two actuator fingers of different curvature radius, the values of $m\sigma_2 - \sigma_1$ for both cases could be calculated based on equation (1). A consistent value of 1.0 GPa for $m\sigma_2 - \sigma_1$ is obtained. Hence, the desired actuator finger shape could be approached via tuning the Cr/Al thickness ratio. The radius

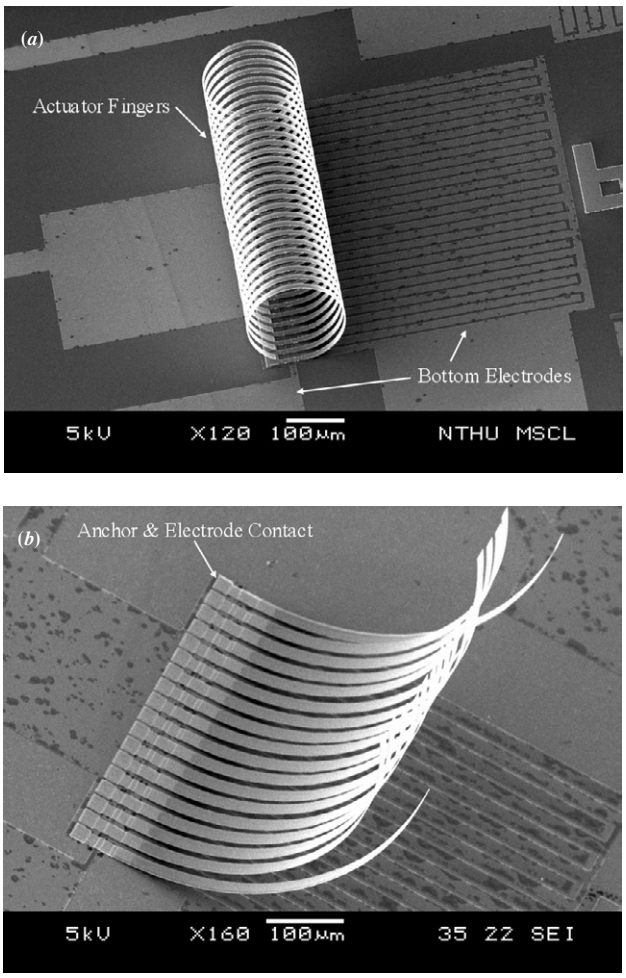

Figure 13. SEM images of our electrostatic micro-actuators. (*a*) The curled actuator fingers (5 μm in width, 5 μm in spacing, 0.8 μm/0.1 μm in Al/Cr thickness and 100 μm in radius of curvature). (*b*) The vertically standing actuator fingers (20 μm in width, 10 μm in spacing, 0.8 μm/0.015 μm Al/Cr thickness and 300 μm in radius of curvature).

of curvature predicted by the theoretical analysis agrees with the experimental observation, except the first and last fingers in figure 13(*b*), which have a larger radius of curvature than the rest. A possible reason for this might result from non-uniform deposition and release processes. This issue could be a problem for the large array design in the future because of lower pull-in voltage. For our case, this problem should be resolved or reduced using a higher quality clean-room facility.

5.2. Frequency response

For dynamics characterization, a Polytec laser Doppler vibrometer (LDV) is used to measure the resonant frequency of the curled finger in air instead of in liquid. The first reason for resonance measurement in air is that the laser light signal of the Polytec LDV scatters on the liquid surface and gives rise to an unreadable signal. The second reason is that the curled finger becomes an overdamped dynamic system in liquid instead of an underdamped system in air. The resonant peak for such an overdamped system is difficult to observe. From system dynamics, the vibration mode is expected to shift to a slightly higher frequency in liquid than in air. The shift is related to the quality factor. Thus, the resonant measurement in air is utilized to study the dynamics of the curled finger actuator. The input for actuating curled fingers is an impulse shock of a hammer by mechanical knocks on the stage to excite all the frequency components of the actuator finger, which is 5 μm in width, 0.8 μm in thickness and 100 μm in radius of curvature. Then, the displacement spectrum is measured. Theoretically, mode 2 is an in-plane vibration. In practice, the fingers could be operated slightly out-of-plane due to horizontal misalignment. Therefore, vertical vibration for the second vibration mode could still be picked up. The measurement result in figure 14 indicates that the first vibration mode of the actuator finger occurs at $f = 6.4$ kHz, the second vibration mode of the actuator finger occurs at $f = 23.4$ kHz and the third vibration mode occurs at $f = 46.8$ kHz. Compared to the second mode, the first vibration mode has a lower Q because the first mode is a vertical vibration mode and struggles with higher air damping caused by a larger moving surface area. Since the finger is driven by external hammer shock, the displacement is quite small compared with low frequency noise in our testing setup. All the experimental results for the resonant frequencies are close to the simulation results (6.8 kHz for the first mode). The small differences between experimental results and simulation predictions come from microfabrication variations and the parameter uncertainties of material properties.

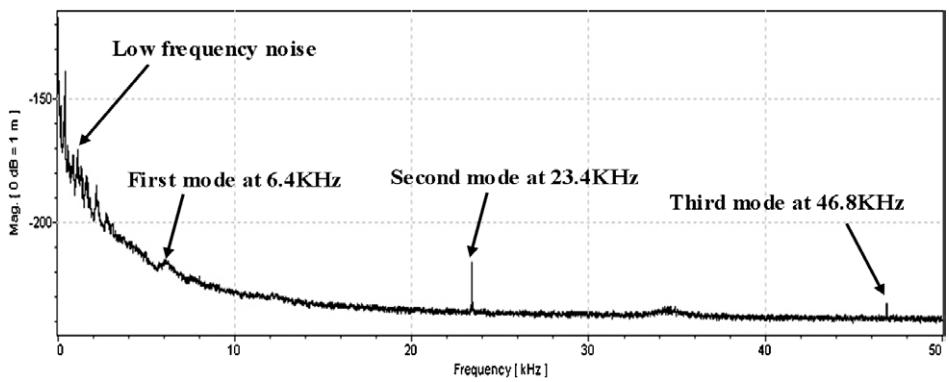

Figure 14. Resonant frequency measurement for the actuator finger.

5.3. Driving testing

The micro-actuator testing is carried out in different liquid environments, including water, 3M^{TM} Fluorinert^{TM} and dimethyl sulfoxide (DMSO). Both Fluorinert and DMSO have lower electrical conductivity than water. Fluorinert liquid with a viscosity similar to water is non-irritating to the eyes and skin, and non-toxic orally. DMSO has properties similar to body fluid and could be used for low temperature cell handling. When a dc voltage is applied on the bottom electrodes, the actuator fingers deflect and zip along the bottom electrodes. The zipping distance depends on the applied voltage, actuator finger stiffness and its original curled shape (radius of curvature). For our present version of actuator fingers (100 μm in radius of curvature, as shown in figure 13(*a*)), a $\sim$10 μm zipping distance is observed with a 100 V dc applied voltage. When the applied voltage is removed, the actuator fingers would return to their original positions. The zipping speed of our actuator fingers could be controlled by the slope of our ramp input signal. The driving voltage in the present experiment is above 90 V. This high voltage results in electrolysis bubbles which randomly occur around some actuator fingers and bottom electrodes for some device testing in water. Instead of water, the testing in both Fluorinert liquid and DMSO is successful. The actuator finger testing in Fluorinert iquid is exhibited to avoid electrolysis bubbles and demonstrates the function of our actuator on micro-object manipulation in the next section. The biomimetic fingers could not be controlled precisely and smoothly due to the pull-in effect and hysteresis characteristics of electrostatic actuation. Further studies and improvements are ongoing.

5.4. Manipulation of micro-object

To demonstrate the actuating function of our curled actuator fingers, several micro-particles are employed. This experiment takes into account the particle–flow interaction that had not been modeled in the above-simplified simulation due to the complications in modeling the complete electro-mechanical–particle-fluidic interaction. Figure 15 shows a series of still images of a row of actuator fingers manipulating/capturing a single particle in a liquid environment (3M^{TM} Fluorinert^{TM}). The particle, marked by a circle, is $\sim$3 μm in diameter. The actuator fingers are 5 μm in width and 5 μm in spacing. The tiny zipping motion ($\sim$5 μm) of the actuator fingers on the left of the particle can be indicated by the two large-deflection ($\sim$100 μm movement) actuator fingers near the bottom of each frame. In figure 15(*a*), the actuator fingers begin to move toward the particle under a ramp applied voltage up to 80 V. Then, the actuator fingers zip along the bottom electrode while the voltage increased up to 100 V, as shown in figure 15(*b*). In figure 15(*c*), the actuator fingers pull back and draw the particle near, when the applied voltage is removed gradually. Finally, in figure 15(*d*), the actuator fingers move back to their original position without any applied voltage. The particle is now moved to the left. The time interval between each frame is 0.1 s. The total time period for these successive frames, shown in figure 15, is less than half a second. During operation, the voltages ($\sim$100 V) are applied sequentially to the odd and even bottom electrodes and then removed simultaneously. In each cycle, the particle was pulled closer to our biomimetic fingers, and finally trapped by the actuator fingers.

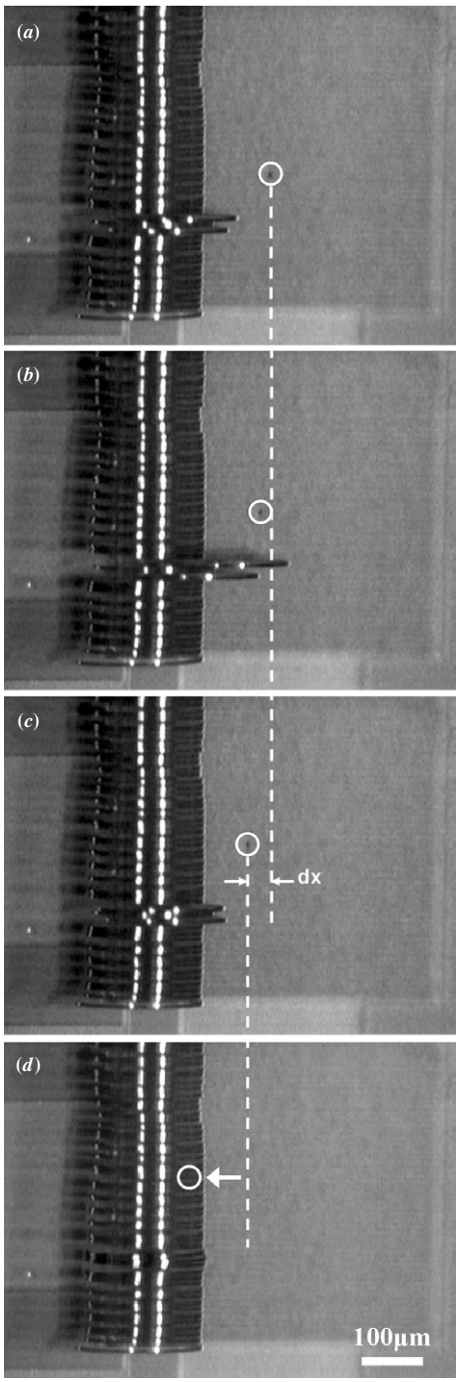

Figure 15. Successive frames taken from a video of manipulating a single particle in liquid environment (3M^{TM} Fluorinert^{TM}). The particle, marked by a circle, is $\sim$3 μm in diameter. The actuator fingers are 5 μm in width and 5 μm in spacing. The time interval between each frame is 0.1 s. (*a*) The actuator fingers start to move toward the particle under a ramp applied voltage up to 80 V. (*b*) The actuator fingers zip along the bottom electrode while the voltage increased up to 100 V. (*c*) The actuator fingers pull back and draw the particle near when the applied voltage is released. (*d*) The actuator fingers move back to their original position without any applied voltage. The particle is moved to the left.

6. Conclusion

From the viewpoint of controlling Reynolds number variations, the capturing function of lobsters' tiny hairs for designing our micro-actuators is mimicked in this research. Furthermore, the technique development on MEMS bimorph cantilevers and electrostatic cantilever actuators is also utilized to develop the curved-finger actuator, the lobster-hair-like capturing actuator. The high-driving voltage, above 90 V, results in electrolysis bubbles and prohibits our present device from operating in water. Several improvements are taken into account and addressed above. For this paper, the successful testing for this proposed micro-actuator in both Fluorinert liquid and DMSO is reported. Because Fluorinert liquid has a viscosity similar to water, the feasibility and functionality of our micro-actuators are thus demonstrated via the manipulation of a micro-object in Fluorinert liquid. The moving mechanism for our lobster-hair-like capturing actuator looks like the early MEMS work regarding ciliary array motion. However, the operation principle of micro-object manipulation is very different from those of early ciliary motion research. Our device actuates and drives the micro-objects via disturbing the fluid field and manipulating the Reynolds number of the surrounding fluid to achieve the function of micro-object manipulation. To our knowledge, this is the first report of the engineering implementation of such innovative MEMS lobster-tiny-hair-like capturing research. These lobster-tiny-hair-like actuators have the advantage of non-contact and non-invasive features for micro-object manipulation, observation and measurement platform for bio-medical research. With a large micro-actuator array format integrated with an image feedback control mechanism, these parallel massive bio-applications will be the main target in this research to pursue in the future.

Acknowledgments

This research was supported partially by the Nano-technology Research Program of University System of Taiwan, ROC. We acknowledge Professor Long Hsu for research development combined with the optical tweezers technique, Professor Hwan-You Chang and Professor Hwei-Ling Peng for research development in bio-applications, Professor K A Chao for helpful comments and D M Yu for assistance with the experiments. This research was inspired by the talk of U C Berkeley's M A R Kohl given at Stanford University in the year 2000.

References

[1] Strick T, Allemand J -F, Croquette V and Bensimon D 2001 The manipulation of single biomolecules *Phys. Today* **54** 46–60

[2] Ashkin A 2000 History of optical trapping *IEEE J. Sel. Top. Quantum Electron.* **6** 841–56

[3] Nakazawa H, Watanabe Y and Morita O 1997 The two-dimensional micro conveyor: principles and fabrication process of the actuator *Proc. Int. Conf. on Solid-State Sensors and Actuators, Transducers '97 (Chicago, IL, 1997)* pp 33–6

[4] Bühringer K-F, Donald B R and MacDonald N C 1996 Single-crystal silicon actuator arrays for micro manipulation tasks *Proc. IEEE MEMS Workshop '96 (San Diego, CA, 1996)* pp 7–12

[5] Fujita H and Gabriel K J 1991 New opportunities for microactuators *Proc. Int. Conf. on Solid-State Sensors and Actuators, Transducer '91 (San Francisco, CA, 1991)* pp 14–20

[6] Ataka M, Omodaka A, Takeshima N and Fujita H 1993 Fabrication and operation of polyimide bimorph actuators for a ciliary motion system *J. Microelectromech. Syst.* **2** 146–50

[7] Ebefors T, Mattsson J U, Kalvesten E and Stemme G 1999 A robust micro conveyer realized by arrayed polyimide joint actuators *Proc. IEEE MEMS Workshop '99 (Orlando, FL, 1999)* pp 576–81

[8] Suh J W, Darling R B, Bohringer K-F, Donald B R, Baltes H and Kovacs G T A 1999 CMOS integrated ciliary actuator array as a general-purpose micromanipulation tool for small objects *J. Microelectromech. Syst.* **8** 483–96

[9] Kim C-J, Pisano A P and Muller R S 1992 Silicon-processed overhanging microgripper *J. Microelectromech. Syst.* **1** 31–6

[10] Lee A P, Ciarlo D R, Krulevitch P A, Lehew S, Trevino J and Northrup M A 1995 A practical microgripper by fine alignment, eutectic bonding and SMA actuation *Proc. Int. Conf. on Solid-State Sensors and Actuators Transducers '95 (Stockholm, Sweden, 1995)* pp 368–71

[11] Ok J, Chu M and Kim C-J 1999 Pneumatically driven microcage for micro-objects in biological liquid *Proc. IEEE MEMS Workshop '99 (Orlando, FL, 1999)* pp 459–63

[12] Jager E W H, Smela E and Inganäs O 2000 Microfabricating conjugated polymer actuators *Science* **290** 1540–5

[13] Wang X-B, Huang Y, Gascoyne P R C and Becker F F 1997 Dielectrophoretic manipulation of particles *IEEE Trans. Indust. Appl.* **33** 660–9

[14] Kohl M A R, Koseff J R, Crimaldi J P, McCay M, Cooper G T, Wiley M B and Moore P A 2001 Lobster sniffing: antennule design and hydrodynamic filtering of information in an odor plume *Science* **294** 1948–51

[15] Beer F P and Johnston E R 1992 *Mechanics of Materials* 2nd edn (New York: McGraw-Hill)

[16] Judy M W, Cho Y-H, Howe R T and Pisano A P 1991 Self-adjusting microstructures (SAMS) *Proc. IEEE MEMS Workshop '91 (Nara, Japan, 1991)* pp 51–6

[17] Legtenberg R, Gilbert J, Senturia S D and Elwenspoek M 1997 Electrostatic curved electrode actuators *J. Microelectromech Syst.* **6** 257–65

[18] Gere J M 2001 *Mechanics of Materials* 5th edn (Pacific Grove, CA: Brooks/Cole)

[19] Shames I H and Dym C L 1985 *Energy and Finite Element Methods in Structural Mechanics* (New York: McGraw-Hill)

[20] Loudon C, Best B A and Kohl M A R 1994 When does motion relative to neighboring surfaces alter the flow through an array of hairs? *J. Exp. Biol.* **193** 233–54